MTPA Tracking Control of Sensorless IPMSM Based on Square-Wave Voltage Signal Injection

Jiwon Yoo, *Student Member*, *IEEE*, Hyeon-Sik Kim, *Member*, *IEEE*, and Seung-Ki Sul, *Fellow*, *IEEE*

***Abstract*— This paper proposes an online maximum torque-per-Ampere (MTPA) control of an interior permanent-magnet synchronous motor (IPMSM) based on the square-wave voltage signal injection. Because the proposed method does not rely on a position sensor, it is applicable to sensorless IPMSMs. The proposed algorithm consists of a dynamic inductance estimator, frequency-adaptive flux observer, and an MTPA tracking controller. The proposed inductance estimation utilizes the pulsating square-wave voltage injection, which can maximize the injection frequency, and the dynamic performance can be preserved during the signal injection. Through the online flux and inductance estimation, the magnetic saturation of the IPMSM and the temperature variation can be fully considered in the MTPA control. The conventional rotor position estimator is replaced with the MTPA tracking controller, which does not rely on offline commissioning parameters. The proposed algorithm can operate under both the torque control and speed control mode, and accurate torque control on MTPA curve can be achieved. The simulation and experimental results demonstrate that the proposed method accurately tracks the MTPA point up to 200% of the rated torque in the mid-and high-speed region.**

***Index Terms*— Flux observer, inductance estimation, interior permanent-magnet synchronous motors (IPMSM), loss minimization, maximum torque-per-Ampere (MTPA), sensorless control, torque control, voltage signal injection.**

I. Introduction

INTERIOR permanent-magnet synchronous motors (IPMSMs) have been adopted in numerous industrial applications by virtue of their merits, such as high efficiency and high power density. To maximize the efficiency of the drive system, the loss minimization of IPMSMs has also received much research attention. In particular, under the base speed, maximum torque-per-Ampere (MTPA) control, which minimizes the current magnitude while maintaining the desired torque, has been a standard solution for high-efficiency IPMSM drives.

Unlike the surface-mounted permanent-magnet synchronous motors (SPMSMs), in which only the q-axis current contributes to torque generation, the output torque of an IPMSM is concerned with not only the q-axis current but also the d-axis current due to the reluctance torque. In an ideal IPMSM with constant motor parameters, the MTPA current trajectory can be calculated analytically [1]. However, magnetic saturation causes the MTPA trajectory of a real IPMSM to deviate from the ideally calculated trajectory. In addition, the temperature variation during operation changes the flux linkage of the magnet, and this may cause the premade MTPA trajectory to be inaccurate.

To achieve precise MTPA operation regardless of the operating conditions, many studies have been conducted. First of all, the look-up-table (LUT) based method is a general approach that provides robust MTPA control without complex algorithms. However, LUT-based methods require a repetitive and tedious offline test procedure, and the premade LUT data is stored in the microprocessor's memory. And, the parameter variation due to temperature change or manufacturing tolerance may not be considered during offline commissioning. Moreover, if the motor operates without the position sensor, the premade LUT becomes ineffective in enhancing the system efficiency.

To overcome the limitations of LUT-based methods, various online MTPA tracking strategies have been reported. For example, real-time parameter estimation is applied to online MTPA control [2]-[4]. These methods update the motor parameters depending on the operating points and calculate the MTPA point using the updated motor parameters. While these methods have the advantage in that additional signal injection is not required, the rank-deficiency problem forces only a few parameters that have a dominant influence on the MTPA curve to be updated. Moreover, because these methods often neglect the derivative terms of the inductances when calculating the MTPA point, the estimated MTPA point might deviate from the actual MTPA trajectory [5].

Power-perturbation-based methods determine the torque extremum point by perturbing the output power around the operating point. They are subdivided into several research groups depending on the way of power-perturbation. In [6] and [7], a high-frequency current injection is proposed. This method tracks the MTPA point by observing the phase of the power ripple induced by the current angle perturbation. However, since the frequency of the current injection is limited by the current regulation bandwidth, the dynamic performance is limited. Instead of injecting current explicitly, [8]-[13] present the excitation by perturbing the reference frame, which reduces

Manuscript received December 11, 2021; revised February 16, 2022 and April 18, 2022; accepted May 15, 2022. This work was supported in part by the Hyundai Motor Chung Mong-Koo Foundation, in part by the Institute of Engineering Research at Seoul National University, and in part by Technology Development Program to Solve Climate Changes (2021M1A2A2065441) through National Research Foundation (NRF) of Korea, funded by Ministry of Science and ICT. *(Corresponding author: Seung-Ki Sul.)*

Jiwon Yoo and Seung-Ki Sul are with the Department of Electrical and Computer Engineering, Seoul National University, Seoul, 08826, South Korea (e-mail: jiwon.yoo@eepel.snu.ac.kr; sulsk@snu.ac.kr).

Hyeon-Sik Kim is with the Department of Electrical Engineering, Gachon University, Seongnam 13120, South Korea (e-mail: hyeonsik@gachon.ac.kr).

the power and speed ripple compared with high-frequency current injection. However, this method assumes that the output current is regulated to the reference value by the current regulator, and the swinging frequency is also limited by the current control bandwidth [12], [13].

In some research works, the flux perturbation has been considered as an alternative to the current signal injection. The flux perturbation methods can effectively replace the current signal injection in the direct torque control (DTC), which utilizes the stator flux as the control variable [14], [15]. In field-oriented control (FOC), the flux perturbation can be implemented by the voltage angle perturbation [16]. Most flux perturbation methods assume the operating point ripple along the constant torque curve in their theoretical derivation. However, simply perturbing the voltage angle does not guarantee the operating point swinging along the constant torque curve. Thus, these methods require an additional control loop, e.g., the high frequency flux observation or the speed control loop, which limits the injection frequency and makes the flux perturbation difficult to be applied to the torque control application.

The other main research stream is grounded in the flux-model-based derivation of the PMSM [17]-[23]. The MTPA condition is calculated by applying the Lagrange multiplier method. The operating point is converged to the desired MTPA trajectory using numerical methods or an r-θ controller. In [19], Newton's method is employed for tracking MTPA point. In [22], the r-θ controller for MTPA control is proposed and has demonstrated a fast dynamic response. These methods can find the accurate MTPA trajectory even under the magnetic saturation if the dynamic inductances and the flux information are precisely known. However, the dynamic inductance information, which are the partial derivatives of the stator fluxes, is difficult to obtain, because not only must the *d*- and *q*-axis inductances be estimated but also the cross dynamic inductance, requiring a complex signal injection method [20], [23] or offline test procedure [21]. Moreover, since the injected signal should be aligned with the actual *d*- and *q*-axis of the rotor reference frame (RRF), it is difficult to implement these methods with the sensorless drives [20].

If the rotor position information is available, MTPA tracking control is usually performed by adjusting the current reference magnitude I_s^* and the current reference angle β^*, while the current regulation is conducted at the RRF. However, because the rotor position is unknown in the sensorless IPMSM, there is no firm reference angle for current angle determination. This renders sensorless MTPA control challenging.

Some studies have combined conventional sensorless control algorithms with online MTPA tracking control [24]. In another study, instead of changing the current angle reference, the *q*-axis inductance in the sensorless observer was artificially modified to change the actual current angle [25]. However, since the dynamics of the sensorless observer and the *q*-axis inductance modifier are intertwined, it not only makes the stability analysis complicated but also increases the control complexity. Moreover, since most sensorless observers are vulnerable to the motor parameter mismatch, the control robustness often deteriorates.

This paper proposes an MTPA criterion that can be calculated at an arbitrary reference frame. Through analysis, a simple MTPA criterion can be formulated at the reference frame synchronized to the current vector, which is utilized as the estimated MTPA reference frame (EMRF) in this paper. At the EMRF, the MTPA criterion only requires the *d*-axis dynamic inductance term, which can be extracted by injecting a single square-wave voltage signal. In the proposed inductance estimation, the direction of the injected voltage signal is adaptively changed to extract the *d*-axis inductance at the EMRF. Through the proposed signal injection, the frequency of the voltage injection is extended to half of the switching frequency.

Based on the proposed MTPA criterion, direct MTPA tracking control (DMTC) for sensorless IPMSM is proposed. This DMTC directly chases the MTPA operating point without estimating the rotor position. The current reference angle is fixed at the *q*-axis of the EMRF. And, the current regulation is also conducted in the EMRF. To accomplish online MTPA control, an MTPA tracking controller adjusts the EMRF to make the output current be on the MTPA operating point.

In addition to the proposed inductance estimator, a flux observer and an MTPA tracking controller are required for the implementation of the proposed method. Unlike the flux perturbation method, the proposed DMTC only requires the fundamental flux observation, which can be calculated by the fundamental components of the output voltage. For the stator flux observer, a frequency adaptive flux observer at the EMRF is adopted in this paper [27], [28]. The MTPA tracking controller consists of a current magnitude controller and an MTPA angle tracking observer. By adjusting the current magnitude and the reference angle of the EMRF, the accurate torque control at MTPA can be achieved.

II. MTPA Condition In The Rotor Reference Frame

The electrical model of the IPMSM can be expressed at the rotor reference frame as follows:

$$\mathbf{v}_{\mathbf{dq}}^{\mathbf{r}} = R_s \mathbf{i}_{\mathbf{dq}}^{\mathbf{r}} + \omega_r \mathbf{J} \boldsymbol{\lambda}_{\mathbf{dq}}^{\mathbf{r}} + \frac{d}{dt} \boldsymbol{\lambda}_{\mathbf{dq}}^{\mathbf{r}} \tag{1}$$

where R_s stands for the stator resistance, and ω_r for the rotor speed. $\mathbf{v}_{\mathbf{dq}}^{\mathbf{r}}$, $\mathbf{i}_{\mathbf{dq}}^{\mathbf{r}}$, and $\boldsymbol{\lambda}_{\mathbf{dq}}^{\mathbf{r}}$ denote the stator voltage, current and flux vector, respectively. The superscript 'r' indicates the RRF. In (1), $\mathbf{J}$ denotes the 90° rotation matrix, i.e., $\mathbf{J} = \begin{bmatrix} 0 & -1 \\ 1 & 0 \end{bmatrix}$.

In this paper, the variable in bold implies the *dq* column vector, e.g., $\mathbf{v}_{\mathbf{dq}}^{\mathbf{r}} = \begin{bmatrix} v_d^r \\ v_q^r \end{bmatrix}$. From (1), the output torque T_e of the IPMSM can be expressed as

$$T_e = 1.5P \mathbf{i}_{\mathbf{dq}}^{\mathbf{r}\,\mathbf{T}} \mathbf{J} \boldsymbol{\lambda}_{\mathbf{dq}}^{\mathbf{r}} \tag{2}$$

where the superscript '$\mathbf{T}$' is the transpose operator, and P is the number of pole pairs. Since the MTPA operating condition means the current vector minimizing its magnitude under a

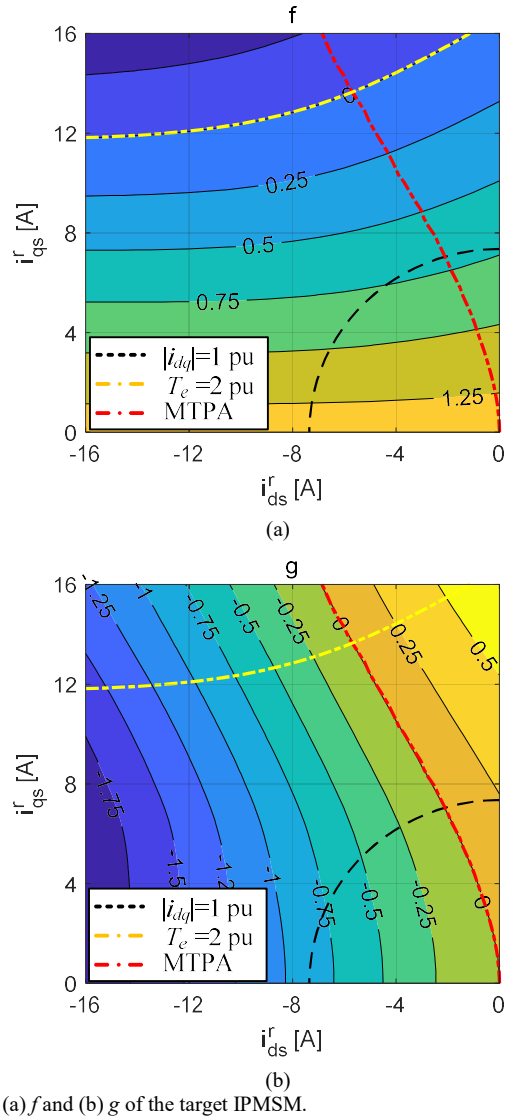

Fig. 1. (a) f and (b) g of the target IPMSM.

given torque reference, the MTPA condition can be stated by the following optimization problem.

$$\text{Minimize } \| \mathbf{i}^{\mathbf{r}}_{\mathbf{dq}} \|, \text{ subject to } T_e^* = 1.5P \mathbf{i}^{\mathbf{r}\,\mathrm{T}}_{\mathbf{dq}} \mathbf{J} \boldsymbol{\lambda}^{\mathbf{r}}_{\mathbf{dq}} \tag{3}$$

where T_e^* is the torque reference. Eq. (3) can be solved by the Lagrange multiplier method as

$$\mathcal{L}\left(i_d^r, i_q^r, \mu\right) = \| \mathbf{i}^{\mathbf{r}}_{\mathbf{dq}} \|^2 + \mu \left(\mathbf{i}^{\mathbf{r}\,\mathrm{T}}_{\mathbf{dq}} \mathbf{J} \boldsymbol{\lambda}^{\mathbf{r}}_{\mathbf{dq}} - \frac{2}{3P} T_e^* \right). \tag{4}$$

The gradient of $\mathcal{L}$ can be represented as

$$\nabla_{i_d^r, i_q^r, \mu} \mathcal{L}\left(i_d^r, i_q^r, \mu\right) = \begin{bmatrix} \frac{\partial}{\partial i_d^r} \mathcal{L}\left(i_d^r, i_q^r, \mu\right) \\ \frac{\partial}{\partial i_q^r} \mathcal{L}\left(i_d^r, i_q^r, \mu\right) \\ \frac{\partial}{\partial \mu} \mathcal{L}\left(i_d^r, i_q^r, \mu\right) \end{bmatrix} = \mathbf{0} \tag{5}$$

where

$$\frac{\partial}{\partial i_d^r} \mathcal{L}\left(i_d^r, i_q^r, \mu\right) = 2 i_d^r + \mu \left(L_{dh} i_q^r - \lambda_q^r - L_{qdh} i_d^r \right) = 0 \tag{6}$$

$$\frac{\partial}{\partial i_q^r} \mathcal{L}\left(i_d^r, i_q^r, \mu\right) = 2 i_q^r + \mu \left(\lambda_d^r + L_{dqh} i_q^r - L_{qh} i_d^r \right) = 0 \tag{7}$$

TABLE I.
NOMINAL MOTOR PARAMETERS

Parameter	Value	Unit
Rated power	1.5	kW
Rated torque ($T_{e,rated}$)	4.1	N·m
Base speed	3500	r/min
Rated current	5.2	A_{rms}
DC-link voltage	311	V
Pole/slot	8/9	
Stator resistance (R_s)	0.84	Ω
Flux linkage of permanent-magnet (λ_f)	88.4	mWb
d-axis static inductance (L_{ds}) @ T_e=2 pu	6.3	mH
q-axis static inductance (L_{qs}) @ T_e=2 pu	8.5	mH

$$\frac{\partial}{\partial \mu} \mathcal{L}\left(i_d^r, i_q^r, \mu\right) = i_q^r \lambda_d^r - i_d^r \lambda_q^r - \frac{2}{3P} T_e^* = 0. \tag{8}$$

In (6)-(8), L_{dh}, L_{qh}, L_{dqh}, and L_{qdh} denote the dynamic inductances, which are the Jacobian matrix of $\boldsymbol{\lambda}^{\mathbf{r}}_{\mathbf{dq}}$ respect to $\mathbf{i}^{\mathbf{r}}_{\mathbf{dq}}$, as follows:

$$\mathbf{L}_{\mathbf{h}} = \frac{\partial \boldsymbol{\lambda}^{\mathbf{r}}_{\mathbf{dq}}}{\partial \mathbf{i}^{\mathbf{r}}_{\mathbf{dq}}} = \begin{bmatrix} L_{dh} & L_{dqh} \\ L_{qdh} & L_{dh} \end{bmatrix} = \begin{bmatrix} \frac{\partial \lambda_d^r}{\partial i_d^r} & \frac{\partial \lambda_d^r}{\partial i_q^r} \\ \frac{\partial \lambda_q^r}{\partial i_d^r} & \frac{\partial \lambda_q^r}{\partial i_q^r} \end{bmatrix}. \tag{9}$$

Because the L_{dqh} is equal to L_{qdh} due to reciprocity, from now on, L_{qdh} is also denoted as L_{dqh}. Eq. (6)-(8) can be condensed into two equations:

$$f = \frac{2}{3P} T_e^* - \mathbf{i}^{\mathbf{r}\,\mathrm{T}}_{\mathbf{dq}} \mathbf{J} \boldsymbol{\lambda}^{\mathbf{r}}_{\mathbf{dq}} = 0. \tag{10}$$

$$g = \mathbf{i}^{\mathbf{r}\,\mathrm{T}}_{\mathbf{dq}} \boldsymbol{\lambda}^{\mathbf{r}}_{\mathbf{dq}} - \left(\mathbf{J} \mathbf{i}^{\mathbf{r}}_{\mathbf{dq}} \right)^{\mathrm{T}} \mathbf{L}_{\mathbf{h}} \mathbf{J} \mathbf{i}^{\mathbf{r}}_{\mathbf{dq}} = 0. \tag{11}$$

The function f indicates whether the torque output matches the desired torque reference, whereas g represents the MTPA condition. Fig. 1(a) and (b) show the functions f and g for the target IPMSM at each operating point, of which the nominal parameters are listed in TABLE I. Fig. 1(a) and (b) are calculated based on the finite element analysis (FEA) results. In Fig. 1(a) and (b), the desired torque reference is set as 2 pu, i.e., T_e^*=2·$T_{e,rated}$, and the corresponding constant torque curve is indicated by the yellow line. The MTPA trajectory is indicated by the red line. It can be noted that f is null where the output torque matches the torque reference.

Similarly, g is null only at the MTPA trajectory, but it is almost zero in the low-current region, regardless of the MTPA condition. To enhance the sensitivity of g to the MTPA condition, $g' = g / \| \mathbf{i}^{\mathbf{r}}_{\mathbf{dq}} \|$ can be used instead [22]. g' is also null only at the MTPA trajectory, as shown in Fig. 2. Therefore, MTPA operation with the desired torque output can be accomplished by solving f = 0 and g' = 0 simultaneously.

However, L_{dh}, L_{qh}, and L_{dqh} are required in the calculation of g'. Since extracting four dynamic inductances at an operating point in real-time is challenging, in [21], the flux or inductance LUT is used instead. Moreover, (10) and (11) are valid in the accurate RRF. Thus, even if L_{dh}, L_{qh}, and L_{dqh} are known, the calculation of f and g' will require accurate rotor position

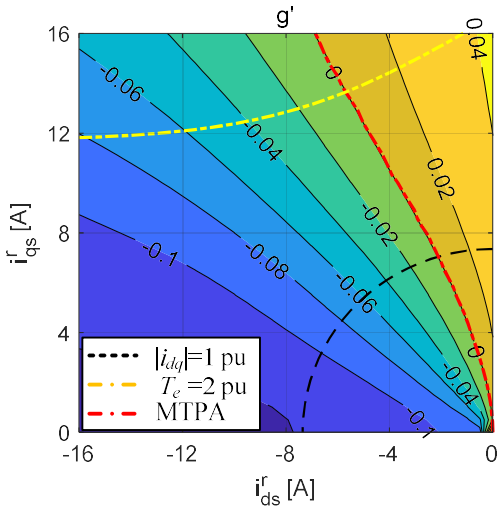

Fig. 2. g' of the target IPMSM.D

information from the position sensor.

III. MTPA Condition at Arbitrary Reference Frame

In the previous section, the MTPA condition was formulated in the conventional RRF. It was concluded that the dynamic inductance information, i.e., L_{dh}, L_{qh}, and L_{dqh}, is required to calculate g. In this section, f and g are recalculated in an arbitrary reference frame, and the optimal reference frame that can most simply represent the MTPA condition is disclosed.

For the arbitrary reference frame 'α', which has a constant angle difference ϕ_0 with the RRF, the current vector diagram can be drawn as Fig. 3. $\mathbf{i}^{\alpha}_{dq}$ can be expressed with $\mathbf{i}^{r}_{dq}$ as

$$\mathbf{i}^{\alpha}_{dq} = \mathbf{R}(-\phi_0)\mathbf{i}^{r}_{dq} \tag{12}$$

where

$$\mathbf{R}(\theta) = \begin{bmatrix} \cos\theta & -\sin\theta \\ \sin\theta & \cos\theta \end{bmatrix}. \tag{13}$$

The dynamic inductances at the α reference frame can be calculated as

$$\mathbf{L}^{\alpha}_{h} = \frac{\partial \boldsymbol{\lambda}^{\alpha}_{dq}}{\partial \mathbf{i}^{\alpha}_{dq}} = \begin{bmatrix} L^{\alpha}_{dh} & L^{\alpha}_{dqh} \\ L^{\alpha}_{dqh} & L^{\alpha}_{dh} \end{bmatrix} = \begin{bmatrix} \frac{\partial \lambda^{\alpha}_{d}}{\partial i^{\alpha}_{d}} & \frac{\partial \lambda^{\alpha}_{d}}{\partial i^{\alpha}_{q}} \\ \frac{\partial \lambda^{\alpha}_{q}}{\partial i^{\alpha}_{d}} & \frac{\partial \lambda^{\alpha}_{q}}{\partial i^{\alpha}_{q}} \end{bmatrix}. \tag{14}$$

From (12), $\mathbf{L}^{\alpha}_{h}$ can be expressed with $\mathbf{L}_{h}$ as follows by the chain rule property of the Jacobian matrix.

$$\mathbf{L}^{\alpha}_{h} = \frac{\partial \boldsymbol{\lambda}^{\alpha}_{dq}}{\partial \boldsymbol{\lambda}^{r}_{dq}} \frac{\partial \boldsymbol{\lambda}^{r}_{dq}}{\partial \mathbf{i}^{r}_{dq}} \frac{\partial \mathbf{i}^{r}_{dq}}{\partial \mathbf{i}^{\alpha}_{dq}} = \mathbf{R}(-\phi_0)\mathbf{L}_{h}\mathbf{R}(\phi_0) \tag{15}$$

where $\partial \boldsymbol{\lambda}^{r}_{dq} / \partial \boldsymbol{\lambda}^{\alpha}_{dq} = \mathbf{R}(-\phi_0)$ and $\partial \mathbf{i}^{r}_{dq} / \partial \mathbf{i}^{\alpha}_{dq} = \mathbf{R}(\phi_0)$, because ϕ_0 is assumed to be constant. Meanwhile, f and g can also be reformulated with $\mathbf{i}^{\alpha}_{dq}$ and $\mathbf{L}^{\alpha}_{h}$ as follows:

$$f = \frac{2}{3P}T_e^* - \mathbf{i}^{\alpha\,\mathrm{T}}_{dq}\mathbf{J}\boldsymbol{\lambda}^{\alpha}_{dq} \tag{16}$$

$$g = \mathbf{i}^{\alpha\,\mathrm{T}}_{dq}\boldsymbol{\lambda}^{\alpha}_{dq} - \left(\mathbf{J}\mathbf{i}^{\alpha}_{dq}\right)^{\mathrm{T}}\mathbf{L}^{\alpha}_{h}\mathbf{J}\mathbf{i}^{\alpha}_{dq}. \tag{17}$$

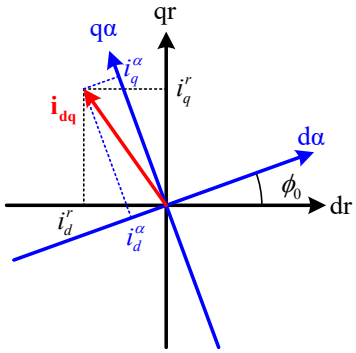

Fig. 3. Relation between $\mathbf{i}_{dq}{}^{r}$ and $\mathbf{i}_{dq}{}^{\alpha}$.

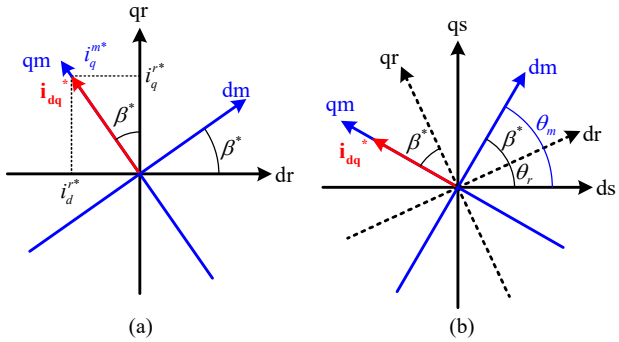

Fig. 4. (a) Estimated MTPA reference frame. (b) Relation between θ_m and θ_r.

Comparing (10) and (11) with (16) and (17), it can be observed that the functions f and g are reference-frame-invariant functions. In other words, f and g can be calculated in any reference frame with the same formulation. Of course, it should be noted that the inductance matrix $\mathbf{L}_{h}$ should also be replaced according to the reference frame change.

In this paper, the EMRF is defined as the reference frame that aligns the q-axis to the current reference vector, as shown in Fig. 4(a). The angle difference between the EMRF and the RRF is the current angle reference β^*. The angle between the EMRF and the stationary reference frame (SRF) is defined as θ_m, as shown in Fig. 4(b). θ_m can be calculated as $\theta_m = \theta_r + \beta^*$, where θ_r is the rotor position. In this paper, the variables in the EMRF are denoted with the superscript 'm'. In the EMRF, the current reference vector can be expressed as

$$\mathbf{i}^{m*}_{dq} = \begin{bmatrix} 0 \\ i^{m*}_q \end{bmatrix} \tag{18}$$

where the superscript '*' denotes the reference value. It should be noted that θ_m is associated with not the actual current but the current reference. It helps θ_m keeping independent of the stator flux and current in the small-signal model. Thus, the calculation in (15) can be applied to the EMRF as well.

Since $i^{m*}_d = 0$, f and g can be simplified in the EMRF as follows, assuming the well-operating current regulation, i.e., $\mathbf{i}^{m*}_{dq} = \mathbf{i}^{m}_{dq}$.

$$f = \frac{2}{3P}T_e^* - \lambda^m_d i^m_q. \tag{19}$$

$$g = i^m_q \lambda^m_q - L^m_{dh} i^{m2}_q. \tag{20}$$

Furthermore, g' can be rewritten as

$$g' = \lambda^m_q - L^m_{dh} i^m_q. \tag{21}$$

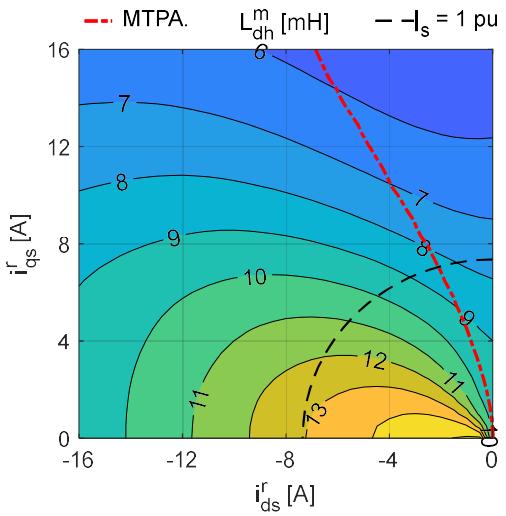

Fig. 5. L^m_{dh} of the target IPMSM.

Compared with (11), the amount of required information is significantly reduced. Instead of the whole dynamic inductance matrix $\mathbf{L}^{\mathbf{m}}_{\mathbf{h}}$, only L^m_{dh} is required. Fig. 5 depicts L^m_{dh} of the target IPMSM. Due to the magnetic saturation, L^m_{dh} is highly nonlinear and varies according to the operating point change. To estimate L^m_{dh} in real-time, a pulsating voltage signal injection method is discussed in the next section. Besides the dynamic inductance, λ^m_d, λ^m_q, and i^m_q can be obtained straightforwardly. i^m_q is nothing but $\| \mathbf{i}^{\mathbf{s}}_{\mathbf{dq}} \|$, and $\boldsymbol{\lambda}^{\mathbf{m}}_{\mathbf{dq}}$ can be obtained from $\boldsymbol{\lambda}^{\mathbf{s}}_{\mathbf{dq}}$.

The calculation in the EMRF eliminates the dependency on the position sensor for the MTPA tracking control. Thus, f and g' in (19) and (21) can be utilized for a sensorless IPMSM, as described in the next section.

IV. Proposed Sensorless MTPA Tracking Control

A. Dynamic Inductance Estimation

If a high-frequency voltage $\mathbf{v}^{\mathbf{m}}_{\mathbf{dqh}}$ is injected, the high-frequency current response can be expressed as

$$\mathbf{v}^{\mathbf{m}}_{\mathbf{dqh}} = \mathbf{L}^{\mathbf{m}}_{\mathbf{h}} \frac{d}{dt} \mathbf{i}^{\mathbf{m}}_{\mathbf{dqh}}. \tag{22}$$

The pulsating square-wave voltage reference at the n-th sampling instant can be represented as

$$\mathbf{v}^{\mathbf{m}}_{\mathbf{dqh}}{}^{*}[n] = \begin{bmatrix} v^{m*}_{dh}[n] \\ v^{m*}_{qh}[n] \end{bmatrix} = \begin{bmatrix} V^{m*}_{dh} \\ V^{m*}_{qh} \end{bmatrix} \cdot clk[n] \tag{23}$$

where $clk[n]$ is the clock signal alternating between -1 and 1 with a specific period T_{inj}. Fig. 6 depicts $clk[n]$ with period 4. V^{m*}_{dh} and V^{m*}_{qh} are the magnitude of the injected voltage signals. $\mathbf{v}^{\mathbf{m}}_{\mathbf{dqh}}{}^{*}[n]$ will be synthesized by the inverter during the time period t=[$(n$+1)T_s, (n+2)T_s], where T_s is the sampling period. Thus, the average output voltage has the waveform of pulsating square-wave with the period of $clk[n]$. The current response at the n-th sampling instant can be represented as

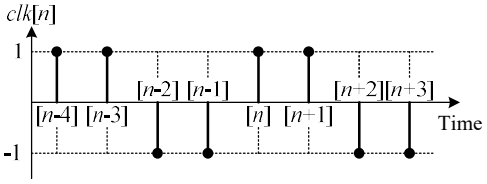

Fig. 6. The waveform of $clk[n]$ with period 4.

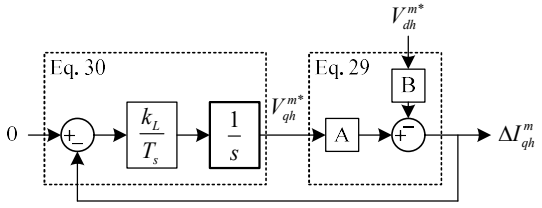

Fig. 7. ΔI^m_{qh} dynamics.

$$\mathbf{v}^{\mathbf{m}}_{\mathbf{dqh}}{}^{*}[n-2] \cdot T_s = \mathbf{L}^{\mathbf{m}}_{\mathbf{h}} \Delta \mathbf{i}^{\mathbf{m}}_{\mathbf{dqh}}[n] \tag{24}$$

where $\Delta \mathbf{i}^{\mathbf{m}}_{\mathbf{dqh}}[n] = \mathbf{i}^{\mathbf{m}}_{\mathbf{dqh}}[n] - \mathbf{i}^{\mathbf{m}}_{\mathbf{dqh}}[n-1]$. In (24), the d-axis equation can be rewritten as

$$v^{m*}_{dh}[n-2] \cdot T_s = L^m_{dh} \Delta i^m_{dh}[n] + L^m_{dqh} \Delta i^m_{qh}[n]. \tag{25}$$

Since $\Delta i^m_{dh}[n]$, $\Delta i^m_{qh}[n]$, and $v^m_{dh}[n-2]$ are the alternating signals, they can be reinterpreted with dc signals by multiplying $clk[n$-2]:

$$V^{m*}_{dh}[n-2] \cdot T_s = L^m_{dh} \Delta I^m_{dh}[n] + L^m_{dqh} \Delta I^m_{qh}[n] \tag{26}$$

where

$$\begin{bmatrix} \Delta I^m_{dh}[n] \\ \Delta I^m_{qh}[n] \end{bmatrix} = \begin{bmatrix} \Delta i^m_{dh}[n] \\ \Delta i^m_{qh}[n] \end{bmatrix} \cdot clk[n-2]. \tag{27}$$

Therefore, if $\Delta I^m_{qh}[n] = 0$, L^m_{dh} can be calculated by dividing $V^{m*}_{dh}[n-2]$ and $\Delta I^m_{dh}[n]$ as follows:

$$L^m_{dh} = \frac{V^{m*}_{dh}[n-2]}{\Delta I^m_{dh}[n]} \cdot T_s. \tag{28}$$

From (24), $\Delta I^m_{qh}[n]$ can be expressed as

$$\Delta I^m_{qh}[n] = \frac{T_s}{\det(\mathbf{L}^{\mathbf{m}}_{\mathbf{h}})} \cdot \left(L^m_{dh} V^{m*}_{qh} - L^m_{dqh} V^{m*}_{dh} \right) \tag{29}$$

where $\det(\mathbf{L}^{\mathbf{m}}_{\mathbf{h}}) = L^m_{dh} L^m_{qh} - L^{m\,2}_{dqh}$. If only V^{m*}_{dh} is injected without V^{m*}_{qh}, $\Delta I^m_{qh}[n]$ would not be zero due to L^m_{dqh}. Thus, to make $\Delta I^m_{qh}[n]$ null, not only V^{m*}_{dh} but also V^{m*}_{qh} should be adequately injected. In this paper, V^{m*}_{qh} is adjusted by integrating $\Delta I^m_{qh}[n]$ as follows:

$$V^{m*}_{qh}[n] = -\frac{T_s z}{z-1} \left(\frac{k_L}{T_s} \Delta I^m_{qh}[n] \right). \tag{30}$$

The z-domain function $T_s \cdot z/(z$-1) is the integral operator, and k_L is a positive gain. The dynamics of $\Delta I^m_{qh}[n]$ can be analyzed by a feedback system in Fig. 7. A and B stand for $\mathrm{A} = T_s \cdot L^m_{dh} / \det(\mathbf{L}^{\mathbf{m}}_{\mathbf{h}})$ and $\mathrm{B} = T_s \cdot L^m_{dqh} / \det(\mathbf{L}^{\mathbf{m}}_{\mathbf{h}})$, respectively. The discrete-time integrator has been replaced with 1/s for simplicity.

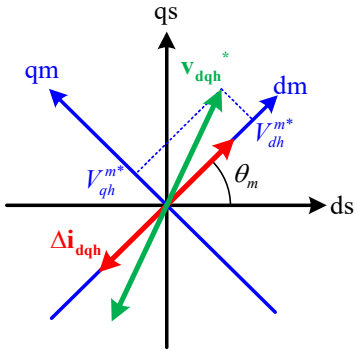

Fig. 8. Pulsating voltage injection to estimate L_{dh}^{m}.

By calculating the feedback loop gain in Fig. 7, ΔI_{qh}^{m} can be expressed as

$$\Delta I_{qh}^{m} \approx -\frac{s}{s+\omega_{cL}}\left(\frac{L_{dqh}^{m}}{\det(\mathbf{L_h^m})}V_{dh}^{m*}\cdot T_s\right) \tag{31}$$

where $\omega_{cL} = k_L \cdot L_{dh}^{m} / \det(\mathbf{L_h^m})$. Since (31) has the form of a high-pass filter, ΔI_{qh}^{m} converges to null by the proposed V_{qh}^{m*} controller. Fig. 8 depicts the relation between the injected voltage signal and the current response. By adjusting V_{qh}^{m*}, there is no Δi_{qh}^{m}, and the pulsating current only exists on the *d*-axis of the EMRF. The sign and magnitude of V_{qh}^{m*} are determined by L_{dqh}^{m}. Thus, L_{dqh}^{m} can be calculated as follows, since $\Delta I_{qh}^{m} = 0$ in (29).

$$\hat{L}_{dqh}^{m} = L_{dh}^{m}\frac{V_{qh}^{m*}}{V_{dh}^{m*}}. \tag{32}$$

$\hat{L}_{dqh}^{m}$ denotes the estimated L_{dqh}^{m}, and it is used in the gain scheduling of the proposed MTPA tracking control. Fig. 9 shows the block diagram of the proposed L_{dh}^{m} estimator. The superscript '^' in $\hat{L}_{dh}^{m}$ stands for the estimated value. Since $\hat{L}_{dh}^{m}$ is calculated from v_{dh}^{m*} and i_{dh}^{m}, V_{dh}^{m*} determines the accuracy of the inductance calculation. Thus, a certain amount of injection voltage should be kept for the *d*-axis of the EMRF.

Regarding the gain setting, k_L should be set as $k_L = \det(\mathbf{L_h^m}) / L_{dh}^{m} \cdot \omega_{cL,desired}$ for the desired bandwidth $\omega_{cL,desired}$. However, it is not easy to calculate $\det(\mathbf{L_h^m})$ online, and a slight mismatch in ω_{cL} deos not deteriorate the inductance estimation performance. Thus, k_L is approximated as $k_L = \hat{L}_{dh}^{m} \cdot \omega_{cL,desired}$ to avoid the use of the preset LUT.

For the accurate inductance estimation, the injection frequency and voltage magnitude should be carefully selected. As the injection frequency is getting higher, the dynamic performance would be enhanced. Also, unwanted interferences with unmodelled harmonic components, e.g., spatial harmonics, could be avoided. Assuming the double sampling at each switching period, the switching frequency injection would be

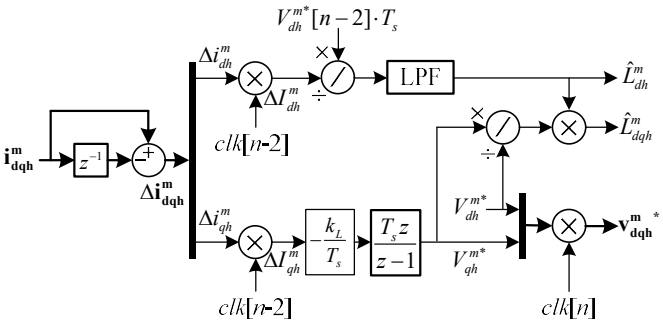

Fig. 9. Block diagram of the dynamic inductance estimator.

the maximum injection frequency. However, it has been analyzed that the switching frequency injection is vulnerable to the inverter nonlinearity effects compared to the half switching frequency injection [29]. Therefore, the half of the switching frequency is selected for the injection in this paper.

The injection voltage magnitude should be determined considering the trade-off between the estimation accuracy and the voltage margin for the fundamental current control. As V_{dh}^{m*} increases, the voltage distortion due to the inverter nonlinearity effects is relatively reduced, and the estimation accuracy can be enhanced. However, an excessive V_{dh}^{m*} requires more voltage margin in the dc-link voltage, so that the base speed for the MTPA operation could be limited. Thus, it is sensible to select the smallest V_{dh}^{m*}, unless the estimation performance is degraded.

B. Stator Flux Estimation

In addition to the dynamic inductance, stator flux information should be obtained for *f* and *g'* calculation. Except for the very low-speed region, the stator flux can be expressed by integrating the back electromotive force (EMF), as follows:

$$\hat{\boldsymbol{\lambda}}_{\mathbf{dq}}^{\mathbf{s}} = \frac{1}{s}\mathbf{e}_{\mathbf{dq}}^{\mathbf{s}} \tag{33}$$

where $\mathbf{e}_{\mathbf{dq}}^{\mathbf{s}} = \mathbf{v}_{\mathbf{dq}}^{\mathbf{s}} - R_s\mathbf{i}_{\mathbf{dq}}^{\mathbf{s}}$. The superscript 's' denotes the SRF. However, (33) asks for the pure integrator, which would be vulnerable to the dc offset error. Moreover, $\mathbf{e}_{\mathbf{dq}}^{\mathbf{s}}$ would contain unwanted ripple terms, such as spatial harmonics of IPMSM.

The issues of the pure integration can be solved by cascading the frequency-adaptive band-pass filter on $\mathbf{e}_{\mathbf{dq}}^{\mathbf{s}}$ as follows:

$$\hat{\boldsymbol{\lambda}}_{\mathbf{dq}}^{\mathbf{s}} = \frac{2\zeta\omega_r}{s^2+2\zeta\omega_r s+\omega_r^2}\mathbf{e}_{\mathbf{dq}}^{\mathbf{s}} \tag{34}$$

where ζ is the damping factor which determines the pass-band of the filter [27]. $\hat{\boldsymbol{\lambda}}_{\mathbf{dq}}^{\mathbf{s}}$ is the estimated stator flux at the SRF. Thanks to the band-pass filter, the harmonic components and the dc offset can be effectively rejected without a phase delay in the fundamental flux estimation. In [28], the discretization error of (34) was analyzed, and the discrete-time frequency-adaptive flux observer (DFAO) was proposed.

This paper adopts the DFAO in [28]. Although the original DFAO calculates the stator flux at the RRF, the stator flux at the EMRF can be obtained by replacing the angle input with θ_m, which is the reference angle of EMRF. Fig. 10 depicts the block

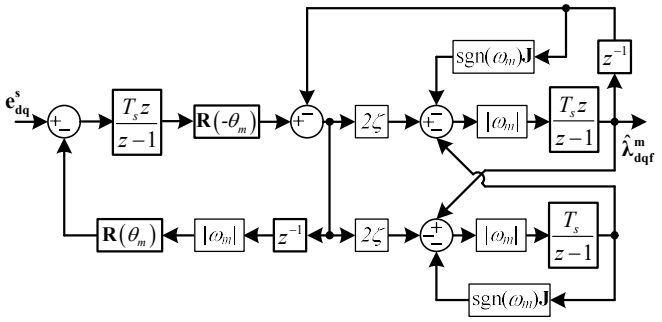

Fig. 10. Block diagram of the frequency-adaptive flux observer.

diagram of the DFAO. ω_m denotes the time derivative of θ_m, which is the speed of the EMRF. sgn(x) is the sign of x. The unique motor parameter used in DFAO is R_s, and it does not require motor inductance information nor flux linkage of the permanent magnet λ_f. R_s can be identified during offline commissioning, and the small discrepancy in R_s identification barely affects $\hat{\boldsymbol{\lambda}}^{\mathbf{m}}_{\mathbf{dqf}}$ in mid- and high-speed region. Therefore, the DFAO in Fig. 10 can accurately estimate the stator flux, regardless of the motor parameter errors in most operating regions.

Since the DFAO calculates the fundamental stator flux based on the stator voltage reference, the inverter nonlinearity effects may deteriorate the flux estimation accuracy in the low-speed region. As described in the original literature [28], the voltage distortion due to the inverter nonlinearity effects can be compensated by a feedforward term in the voltage reference in order to enhance the flux estimation accuracy [30].

However, a slight R_s error or discrepancies in inverter nonlinearity compensation would have non-negligible effect at very low speed region where the back EMF magnitude is extremely small. Therefore, the operating frequency of the proposed DMTC should be determined considering the R_s tolerance of the system.

C. MTPA Point Tracking Controller

The MTPA condition at the desired torque output can be accomplished by nullifying f and g'. For stable MTPA tracking control, this paper presents an MTPA point tracking controller, as shown in Fig. 11(a) and (b). It consists of two blocks: the current magnitude controller in Fig. 11(a) and the MTPA angle controller in Fig. 11(b). The current magnitude controller consists of an integral controller with anti-windup, similar to [22]. However, the MTPA angle controller has a PI-type phase-locked-loop (PLL) to make θ_m converge to the ramp-increasing MTPA angle θ_{MTPA}. In the proposed angle controller, ω_m, which is used in the DFAO and the current controller, is calculated. In addition, since ω_m is the same as the rotor speed ω_r when ignoring the MTPA angle variation at transients, ω_m can be used as the estimated rotor speed for the speed control input.

In Fig. 11(a) and (b), n_f and n_g are the normalization factors of f and g', respectively, and $k_{p\theta}$, $k_{i\theta}$, and $k_{i\tau}$ are the gains of each controller. The anti-windup gains, $k_{a\tau}$ can be set for the case of saturation [22]. The current magnitude is limited from -I_{max} to I_{max}, where I_{max} is the maximum current level of the system. In the negative torque region, the proposed algorithm operates in

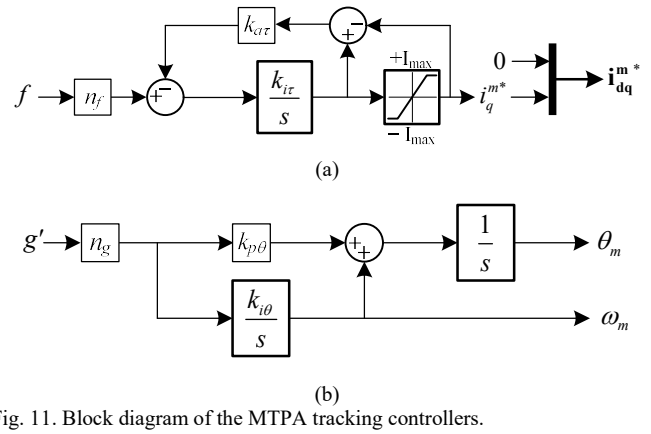

Fig. 11. Block diagram of the MTPA tracking controllers.
(a) Torque controller. (b) MTPA angle tracking controller.

the $i_q^{m*} < 0$ region, and there is no step-change in the controller output. Hence, a seamless transition even at the reversed torque reference can be expected.

Assuming proper normalization, $n_f \cdot f$ and $n_g \cdot g'$ represent the magnitude and angle errors against the desired MTPA operating point, respectively, as

$$n_f \cdot f \approx \tilde{i}_s = i_{s,MTPA} - i_q^{m*} \tag{35}$$

$$n_g \cdot g' \approx \tilde{\theta}_{MPTA} = \theta_{MTPA} - \theta_m \tag{36}$$

where θ_{MTPA} is the MTPA angle and $i_{s,MTPA}$ is the current magnitude for the desired torque output. Subsequently, the dynamics of i_q^{m*} and θ_m can be expressed as

$$i_q^{m*} = \frac{k_{i\tau}}{s + k_{i\tau}} i_{s,MTPA} \tag{37}$$

$$\theta_m = \frac{k_{p\theta} s + k_{i\theta}}{s^2 + k_{p\theta} s + k_{i\theta}} \theta_{MTPA}\,. \tag{38}$$

In (37) and (38), $k_{i\tau}$, $k_{p\theta}$, and $k_{i\theta}$ can be set as

$$k_{i\tau} = \omega_\tau \tag{39}$$

$$k_{p\theta} = 2\zeta_\theta \omega_\theta \tag{40}$$

$$k_{p\theta} = \omega_\theta^{\,2} \tag{41}$$

where ω_τ and ω_θ are the desired bandwidth of the torque and MTPA angle control, respectively, and ζ_θ is the damping factor of the MTPA angle controller.

To calculate n_f and n_g, small-signal modeling of f and g' with respect to $\tilde{i}_s$ and $\tilde{\theta}_{MTPA}$ is conducted. First, the partial derivative of f with respect to $\tilde{i}_s$ is calculated as follows:

$$\frac{\partial f}{\partial \tilde{i}_s} = -\frac{\partial f}{\partial i_q^m} = \lambda_d^m + L_{dqh}^m i_q^m\,. \tag{42}$$

Similarly, the partial derivative of g' with respect to $\tilde{\theta}_{MTPA}$ can be expressed as

$$\frac{\partial g'}{\partial \tilde{\theta}_{MTPA}} = -\frac{\partial g'}{\partial \theta_m} = \lambda_d^m + L_{dqh}^m i_q^m + \frac{\partial L_{dh}^m}{\partial \theta_m} i_q^m\,. \tag{43}$$

For the ideal operation of the proposed algorithm, n_f and n_g should be set as the inverse of $\partial f / \partial \tilde{i}_s$ and $\partial g' / \partial \tilde{\theta}_{MTPA}$,

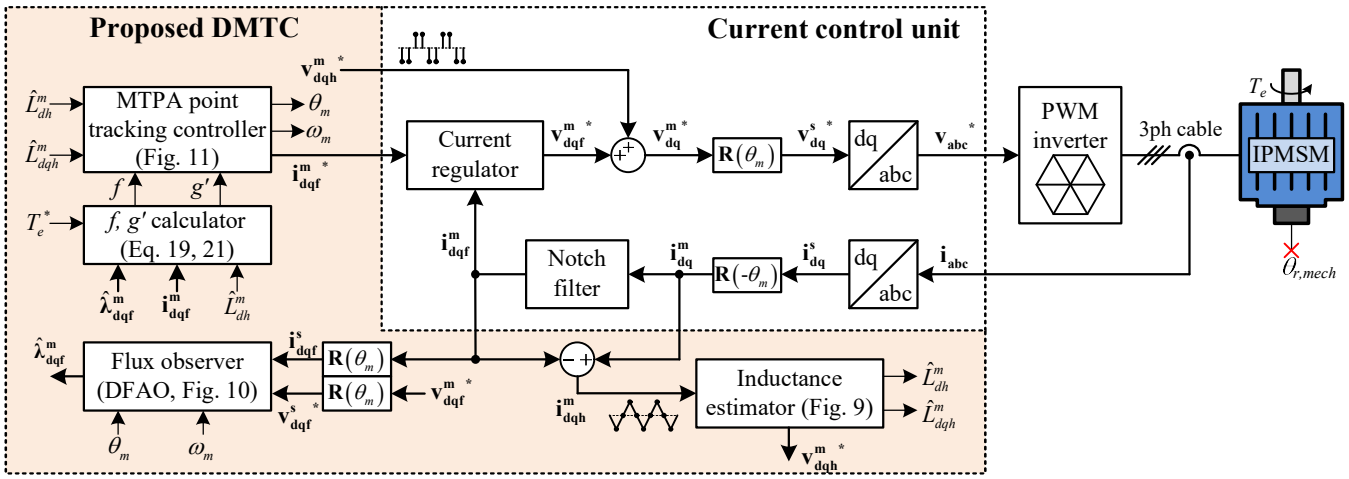

Fig. 12. Control block diagram.

respectively. However, in (43), $\partial g'/\partial\tilde{\theta}_{MTPA}$ contains the derivative of L_{dh}^m to θ_m, which is challenging to estimate in real-time. Although the ideal n_f and n_g can be set through the preset LUT, it may undermine the effectiveness of the proposed online tracking algorithm. Thus, in this paper, n_f and n_g are set identical as follows for the sake of simplicity.

$$n_f = n_g = \frac{1}{\hat{\lambda}_{df}^m + \hat{L}_{dqh}^m i_q^{m*}} \tag{44}$$

where $\hat{\lambda}_{df}^m$ is obtained from the DFAO and $\hat{L}_{dqh}^m$ from (32).

Fig. 12 shows the overall control block diagram of the proposed MTPA tracking algorithm. The current regulator is based on the EMRF, where θ_m is utilized for the coordinate transformation from the SRF. To separate the fundamental frequency component from the phase current information, a notch filter is implemented in the current control unit. The high-frequency current is extracted by subtracting the fundamental current from the measured current to avoid the implementation duplication. The fundamental components are denoted by the subscript 'f', e.g., $\mathbf{v}_{\mathbf{dqf}}^{\mathbf{m}*}$. It should be noted that the proposed MTPA control does not call for the rotor position estimation. Therefore, the addition of a sensorless observer, which is vulnerable to parameter errors, is not required.

D. ω_m-Based Speed Control

As shown in Fig. 12, the torque control mode of the proposed sensorless DMTC can be implemented without the rotor position estimation. However, the absence of the rotor position estimator might make the proposed method difficult to be utilized in the speed control application, which requires the rotor speed as a feedback term.

Fortunately, the proposed MTPA tracking controller provides ω_m information, which can substitute for ω_r. The speed of EMRF in mechanical angle can be calculated as

$$\omega_{m,mech} = \frac{1}{P}\omega_m . \tag{45}$$

The error between $\omega_{m,mech}$ and the mechanical rotor speed $\omega_{r,mech}$ can be expressed as follows:

TABLE II.
CONTROL PARAMETERS

Parameter	Value	Unit
Switching frequency f_{sw}	10	kHz
Sampling frequency f_s	20	kHz
Injection frequency f_{inj}	5	kHz
Damping factor in DFAO (ζ)	3	
Current control bandwidth ω_{cc}	$2\pi\cdot200$	rad/s
ω_τ	$2\pi\cdot50$	rad/s
ω_θ	$2\pi\cdot20$	rad/s
ζ_θ	1.0	
ω_{cL}	$2\pi\cdot100$	rad/s
V_{dh}^{m*}	20	V

$$\omega_{m,mech} - \omega_{r,mech} = -\frac{1}{P}\frac{d}{dt}\operatorname{atan}\left(\frac{i_d^r}{i_q^r}\right). \tag{46}$$

Therefore, the speed error would be proportional to the slew rate of the current angle deviation, and $\omega_{m,mech}$ will converge to $\omega_{r,mech}$ at the steady-state. Moreover, since $\operatorname{atan}(i_d^r/i_q^r)$ does not exceed $\pi/2$ in IPMSMs, the speed error induced by the current angle deviation also would be limited. Assuming the current angle varies from 0 to $\pi/2$ in 100 ms as an extreme case, it would result in 38 r/min transient error for an 8-pole machine. Therefore, $\omega_{m,mech}$ in (45) can be utilized for the speed control application where the steady state speed matters.

V. SIMULATION AND EXPERIMENTAL RESULTS

The effectiveness of the proposed algorithm is verified with simulation and experimental tests. The IPMSM in Fig. 13(a), whose nominal parameters are listed in TABLE I, is selected for the machine under tests. The inverters used in the experimental verification are shown in Fig. 13(b). The control algorithm has been implemented on TMS320F28377D, of which only the single core has been dedicated for driving both the load machine and the target motor. The control parameters used in the simulation and experiments are listed in TABLE II. The switching frequency is set as 10 kHz, and the double sampling is conducted at each switching period. For the simulation, a

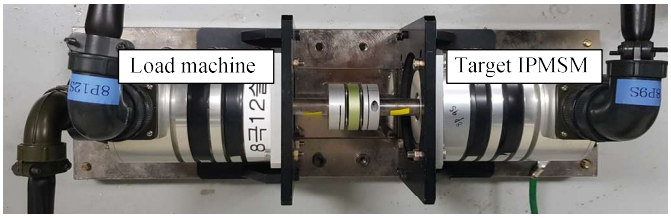

(a)

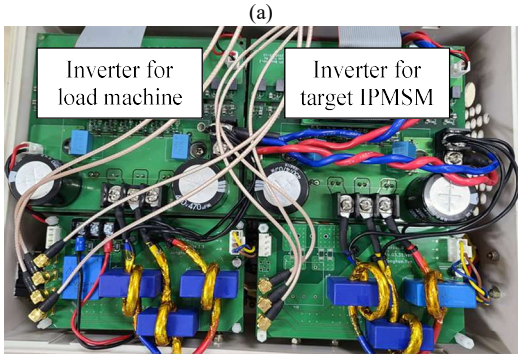

(b)

Fig. 13. (a) Motor-generator set. (b) Inverters used in experiments.

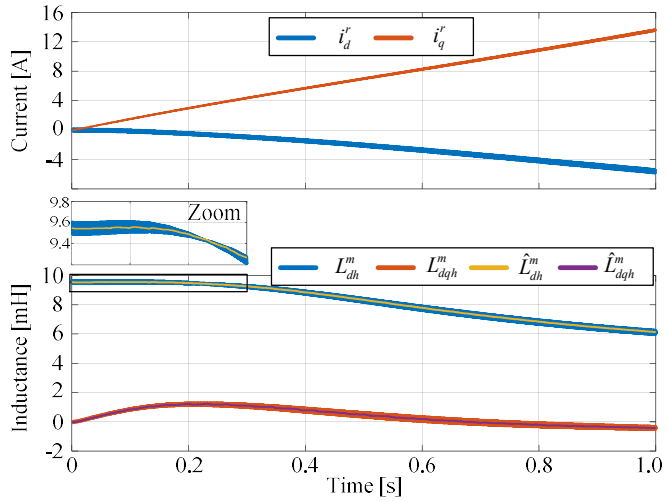

(a)

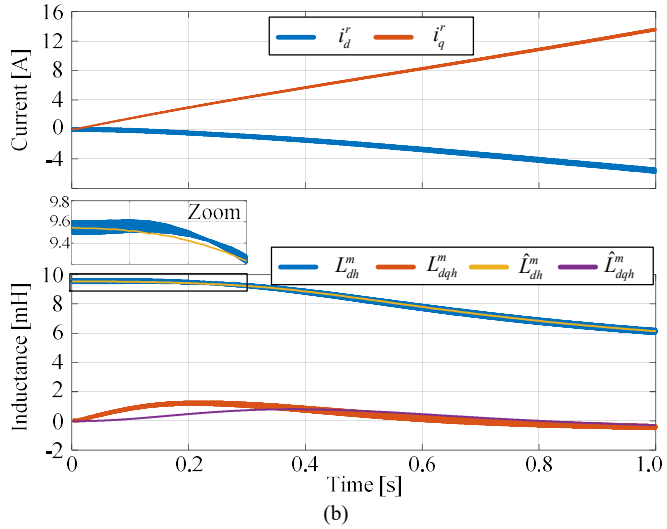

(b)

Fig. 14. Inductance estimation performance (simulation). (a) ω_{cL}=2π·100 rad/s. (b) ω_{cL}=2π·1 rad/s.

high-fidelity IPMSM model constructed by the FEA is implemented through MATLAB/ Simulink [31]. For the current

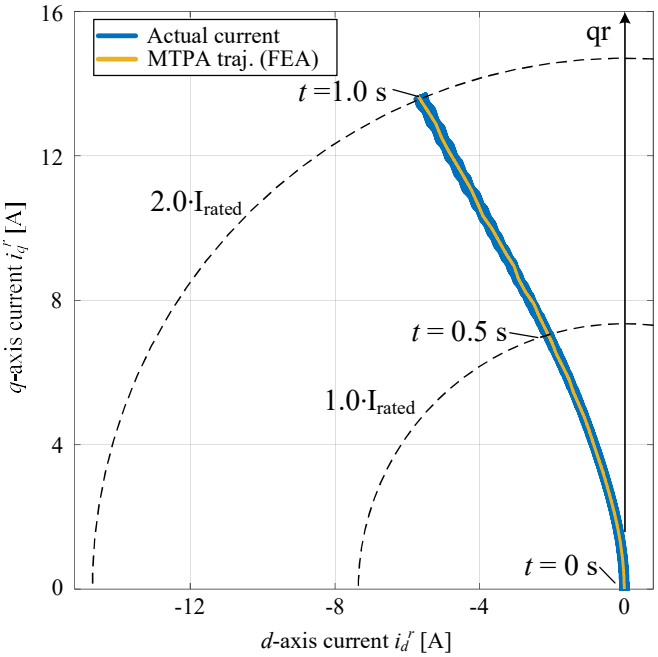

Fig. 15. MTPA tracking performance (simulation).

regulation, the complex-vector current regulator is implemented with the nominal parameters listed in TABLE I [32]. To evaluate the torque control performance, the target IPMSM is controlled in the torque control mode, and the rotor speed is regulated by the load machine. The operating speed is set as 2000 r/min, unless otherwise stated.

A. Simulation Results

Fig. 14(a) and (b) show the results of the inductance estimation. To evaluate only the inductance estimation performance, the target motor is operated with the position sensor and the current reference is calculated from the preset LUT. While the current increases from zero to 2 pu on the MTPA trajectory, $\hat{L}^m_{dh}$ and $\hat{L}^m_{dqh}$ are estimated by the proposed inductance estimator. In Fig. 14(a), ω_{cL} is set as 2π·100 rad/s, which is higher than ω_τ and ω_θ. The results indicate that the proposed inductance estimator accurately calculates the dynamic inductance without delay. Fig. 14(b) demonstrates the result at ω_{cL} = 2π·1 rad/s. Due to the limited bandwidth of ΔI^m_{qh} regulator, $\hat{L}^m_{dqh}$ has a sluggish response, and the non-negligible transient error is observed. Moreover, it can be noticed that the $\hat{L}^m_{dqh}$ error affects the $\hat{L}^m_{dh}$ estimation performance.

The accuracy of the proposed sensorless MTPA control is verified in Fig. 15. From t = 0 s to t = 1 s, the torque reference is increased from zero to 2 pu. The actual current closely tracks the MTPA trajectory, indicated by the yellow line. It can be observed that the actual current is plotted as a thicker line compared with the MTPA trajectory. This is due to the current ripple originating from the square-wave signal injection.

Fig. 16(a) and (b) show the waveforms at the rapid torque reference variation. Twice the rated torque was applied with a slew rate of 20 pu/s. Fig. 16(a) depicts the waveforms under the positive load torque. The actual current in the EMRF is plotted

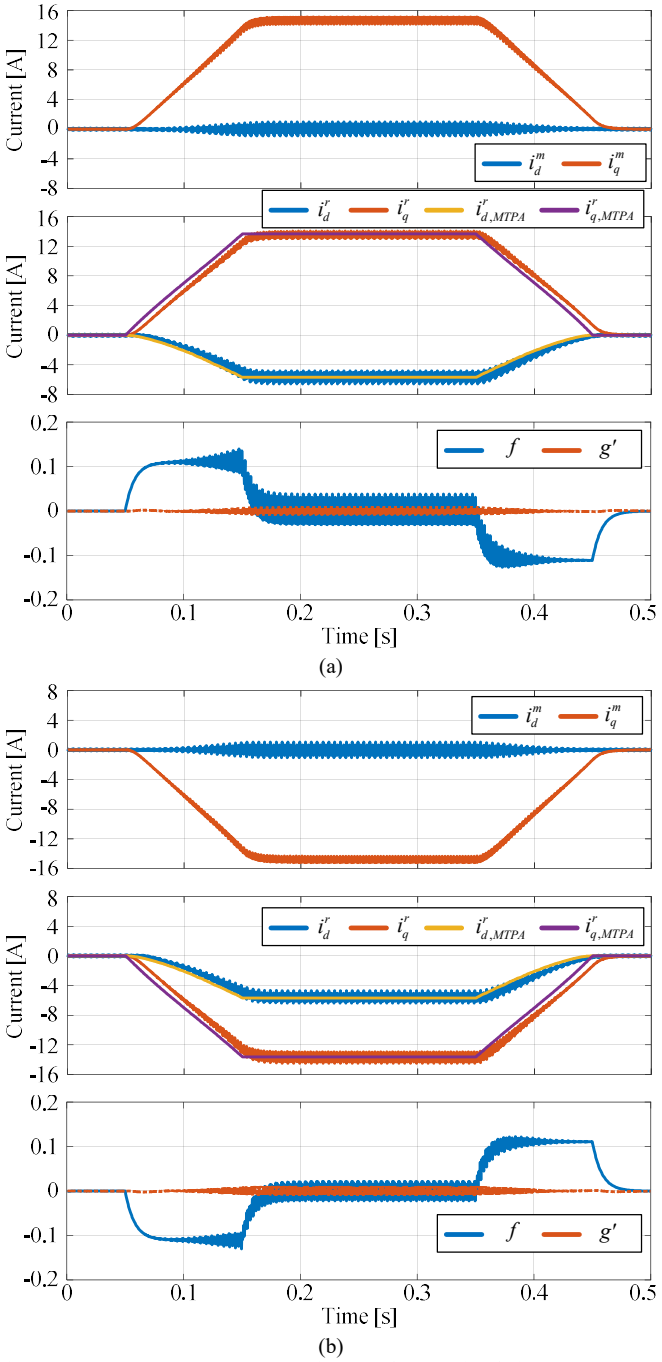

Fig. 16. Current response at torque reference change (simulation).
(a) Positive torque reference. (b) Negative torque reference.

at the top of the figure. The *d*-axis current i_d^m is regulated at null, except for the ripple term. However, in the RRF, the output current closely follows the MTPA trajectory. The functions f and g' are nullified at the steady-state by the proposed MTPA controller. Fig. 16(b) shows the waveform under the negative load torque. Similarly, the actual current is well regulated at the MTPA operating point. It can be noticed that i_q^m is regulated to the negative value to follow the negative torque reference.

B. Experimental Results

To confirm the effect of the injection voltage magnitude on the inductance estimation, the estimation performances under various V_{dh}^{m*} are compared in Fig. 17(a) and (b). The rotor speed is set as 500 r/min. Since the inverter nonlinearity effects have non-negligible impacts in low-current region, $\hat{L}_{dh}^m$ estimation performance is degraded as V_{dh}^{m*} decreases in Fig. 17(a). In the rated load condition, the output current polarity is determined accurately regardless of the high frequency voltage injection, and the effect of inverter nonlinearity on $\hat{L}_{dh}^m$ estimation

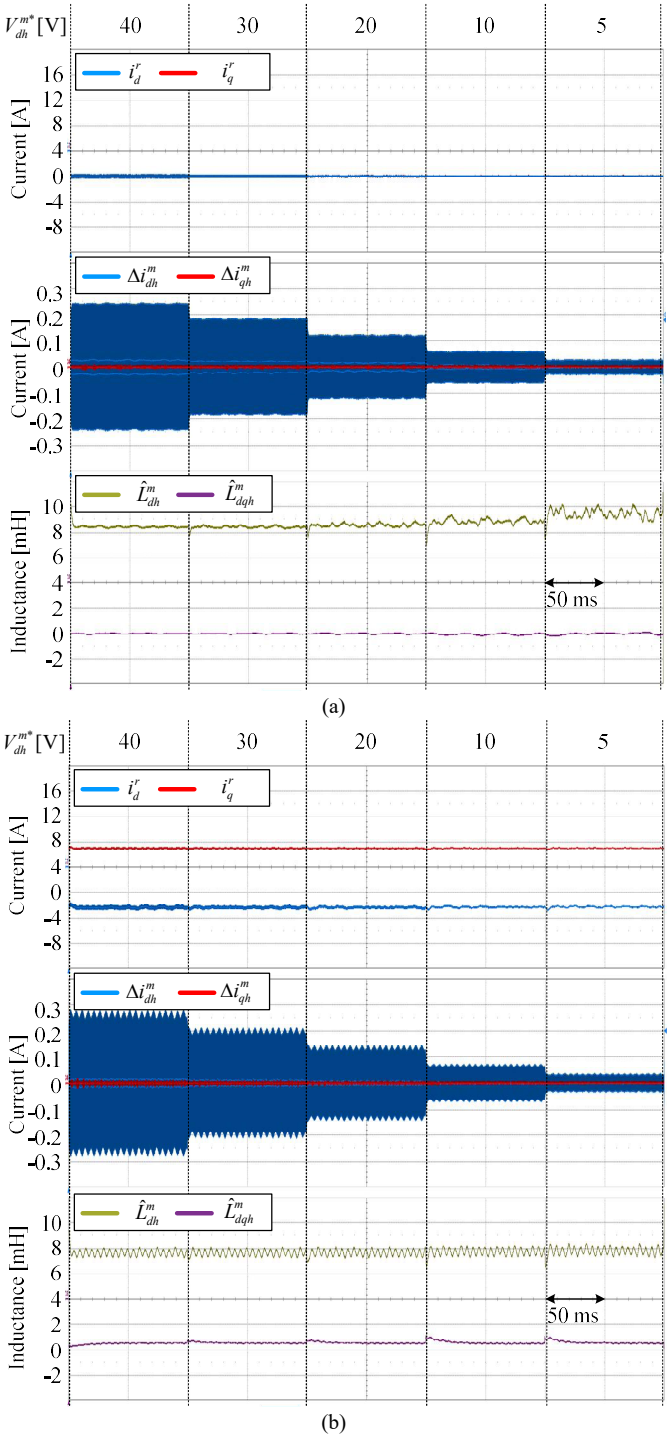

Fig. 17. High frequency current response at various V_{dh}^{m*} (experiments).
(a) No load condition. (b) Rated load condition.

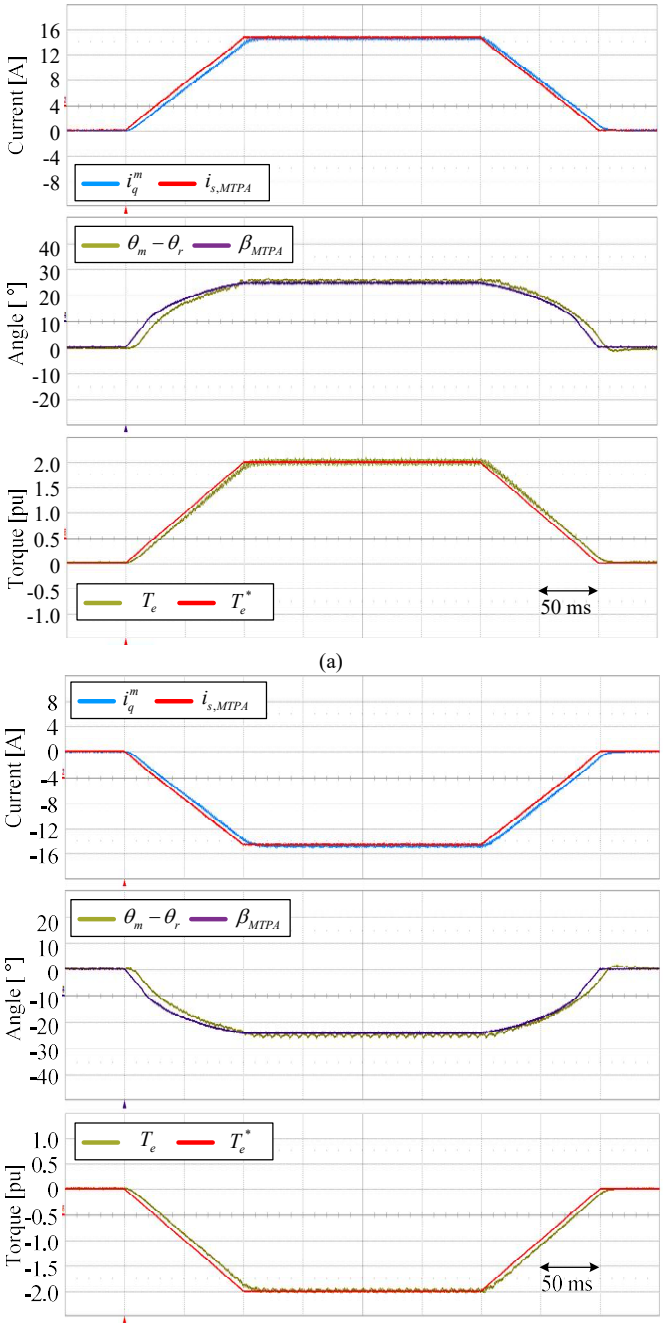

Fig. 18. Current response at torque reference change (experiments). (a) Positive torque reference. (b) Negative torque reference.

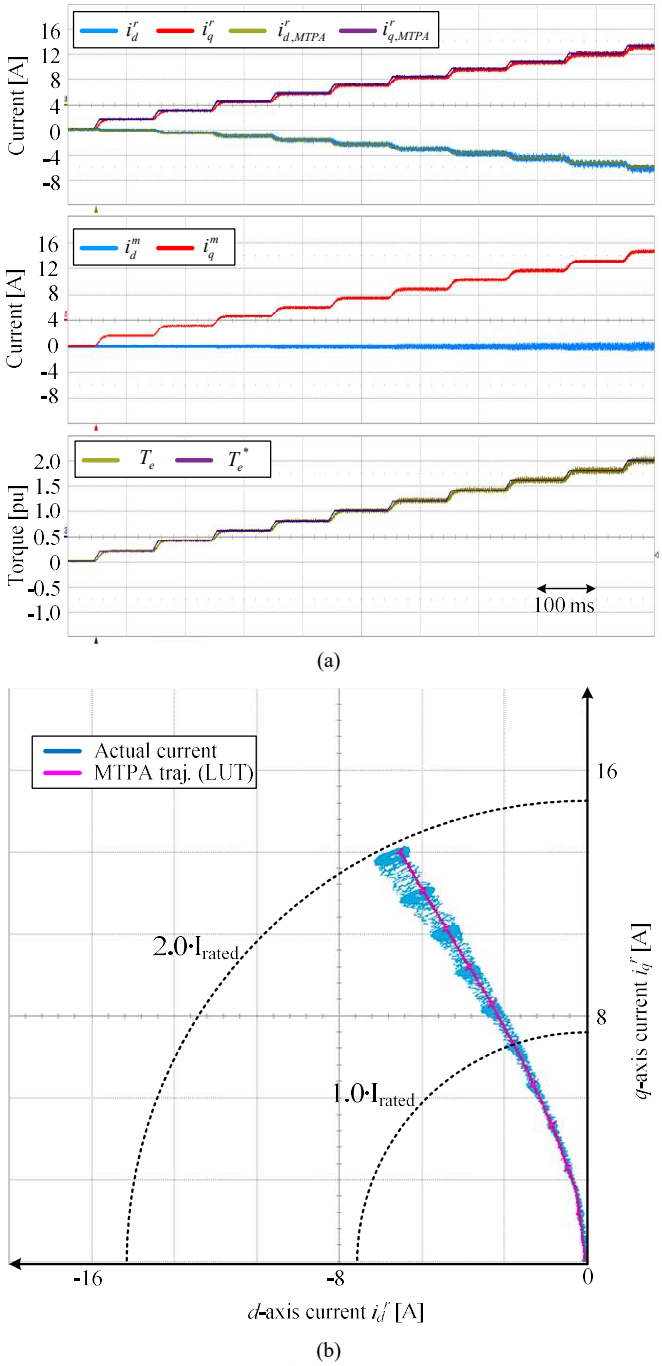

Fig. 19. (a) Current response at gradual torque reference increase (experiments). (b) Lissajous waveform.

performance can be neglected. In the rest parts of the paper, V_{dh}^{m*} is set as 20 V for the consistent performance even at the no load condition.

Fig. 18(a) and (b) depict the experimental waveforms under the torque reference change. As in the simulation, twice the rated torque was applied with the slew rate of 20 pu/s. $i_{s,MTPA}$ and β_{MTPA} are the current magnitude and its angle on the actual MTPA trajectory, respectively, that were extracted experimentally for comparison. Since the DMTC directly controls θ_m, which is continuously changing according to the shaft rotation, θ_m-θ_r is plotted for better visibility. It should be noted that θ_r is plotted simply for monitoring purposes, and it is not used in the proposed algorithm. i_q^m and θ_m-θ_r are well regulated around $i_{s,MTPA}$ and β_{MTPA}. Additionally, the actual torque follows the torque reference T_e^*well. In Fig. 18(b), the actual torque is regulated to the negative torque reference through the negative i_q^m, and it can be noticed that θ_m-θ_r also has a negative angle.

To confirm the MTPA tracking performance in all operating current regions, a gradually increasing torque reference from zero to twice the rated torque is applied as shown in Fig. 19(a) and (b). In Fig. 19(a), the torque response is well regulated to the torque reference. Moreover, the actual current is well regulated to the MTPA trajectory by the proposed algorithm.

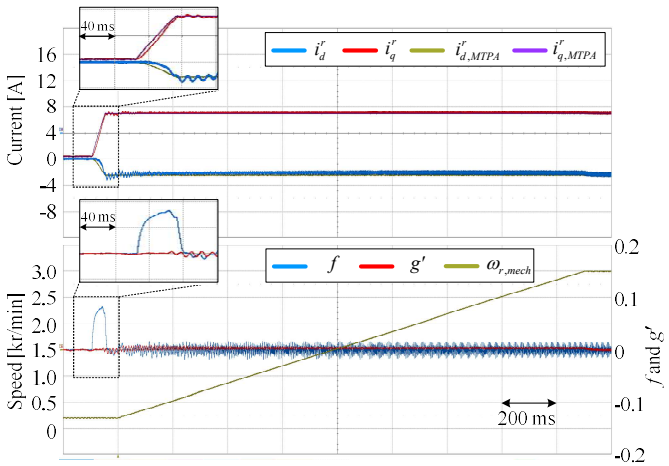

Fig. 20. Current response under speed variation (experiments).

The Lissajous waveforms of the *dq*-axis current are shown in Fig. 19(b). The actual current at the rotor reference frame is calculated from $\mathbf{i}_{\mathbf{dq}}^{\mathbf{m}}$. Although the actual current has a ripple term, the average values of the actual current match well with the MTPA trajectory in all operating ranges.

As mentioned, the experimental verification above was conducted at 2000 r/min. To verify the consistency of the operating point even under speed variation, in Fig. 20, the rotor speed was accelerated from 200 r/min to 3000 r/min by the load machine, and the target IPMSM had consistently produced the rated torque under the proposed sensorless DMTC operation. To show the MTPA tracking performance, $\mathbf{i}_{\mathbf{dq}}^{\mathbf{r}}$ calculated based on the monitored θ_r, which does not engage in the proposed DMTC algorithm, is plotted in Fig. 20. The speed acceleration slew rate was set as 1562 (r/min)/s. The proposed algorithm maintained the MTPA tracking performance even during speed acceleration, and f and g' were well regulated around null.

As analyzed in Section IV. *D*, the proposed DMTC can operate under the speed control mode. In Fig. 21, the target motor regulates the shaft speed with a PI controller. The effective speed control bandwidth is set as 4 Hz. The speed is accelerated from 200 r/min to 3000 r/min in 1.8 s and decelerated to 200 r/min within 5 s. The load machine applies the rated torque at 3000 r/min, and it is released at 200 r/min. the torque slew rate is set as 10 pu/s. It should be noted that the proposed DMTC regulates the speed without losing the MTPA tracking capability. Due to the limited bandwidth of the MTPA tracking controller, the transient speed error is larger than expected in Section IV. *D*. Nevertheless, the error between $\omega_{r,mech}$ and $\omega_{m,mech}$ does not exceed 100 r/min at transients, and there is no steady-state error.

VI. Conclusion

This paper proposes an online maximum torque-per-Ampere (MTPA) tracking control for sensorless interior permanent-magnet synchronous motors (IPMSMs). The proposed method exploits a pulsating square-wave voltage signal injection. The MTPA condition is formulated by the Lagrange multiplier method in an arbitrary reference frame, and it is found that a specific MTPA criterion can be obtained in the arbitrary reference frame. The proposed MTPA control requires the stator flux and the *d*-axis dynamic inductance in the estimated

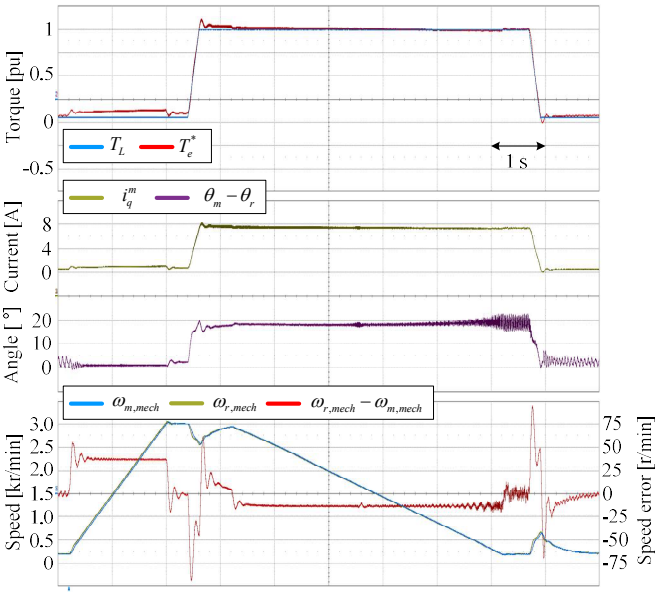

Fig. 21. Waveforms under speed control (experiments).

MTPA reference frame (EMRF), which aligns the current reference to its *q*-axis. The pulsating voltage signal is injected with a tilted injection angle to estimate the dynamic inductance in real-time. The voltage tilting angle is adjusted in real-time by feeding back the pulsating current response. Additionally, the stator flux information is obtained through the discrete-time frequency-adaptive flux observer (DFAO). With the DFAO and the dynamic inductance estimator, the MTPA criterion can be calculated without the rotor position information.

Based on a calculated MTPA criterion, the sensorless MTPA tracking controller, which directly estimates the MTPA angle without having to estimate the rotor position, is designed. The desired bandwidth of the MTPA tracking controller is realized by the online gain scheduling, which does not require any offline commissioning. Moreover, the proposed algorithm does not require any preset look-up table. The feasibility of the proposed MTPA tracking algorithm was verified with a 1.5-kW-rated-IPMSM through simulation and experimental tests.

References

[1] S. Morimoto, M. Sanada and Y. Takeda, "Wide-speed operation of interior permanent magnet synchronous motors with high-performance current regulator," in *IEEE Transactions on Industry Applications*, vol. 30, no. 4, pp. 920-926, July-Aug. 1994, doi: 10.1109/28.297908.

[2] Y. A. -. I. Mohamed and T. K. Lee, "Adaptive self-tuning MTPA vector controller for IPMSM drive system," in *IEEE Transactions on Energy Conversion*, vol. 21, no. 3, pp. 636-644, Sept. 2006, doi: 10.1109/TEC.2006.878243.

[3] Q. Liu and K. Hameyer, "High-Performance Adaptive Torque Control for an IPMSM With Real-Time MTPA Operation," in *IEEE Transactions on Energy Conversion*, vol. 32, no. 2, pp. 571-581, June 2017, doi: 10.1109/TEC.2016.2633302.

[4] F. Lin, Y. Liu and W. Yu, "Power Perturbation Based MTPA With an Online Tuning Speed Controller for an IPMSM Drive System," in *IEEE Transactions on Industrial Electronics*, vol. 65, no. 5, pp. 3677-3687, May 2018, doi: 10.1109/TIE.2017.2762634.

[5] A. Dianov, F. Tinazzi, S. Calligaro and S. Bolognani, "Review and Classification of MTPA Control Algorithms for Synchronous Motors," in *IEEE Transactions on Power Electronics*, vol. 37, no. 4, pp. 3990-4007, April 2022, doi: 10.1109/TPEL.2021.3123062.

[6] S. Kim, Y. Yoon, S. Sul and K. Ide, "Maximum Torque per Ampere (MTPA) Control of an IPM Machine Based on Signal Injection Considering Inductance Saturation," in *IEEE Transactions on Power*

Electronics, vol. 28, no. 1, pp. 488-497, Jan. 2013, doi: 10.1109/TPEL.2012.2195203.
[7] S. Bolognani, R. Petrella, A. Prearo and L. Sgarbossa, "Automatic Tracking of MTPA Trajectory in IPM Motor Drives Based on AC Current Injection," in *IEEE Transactions on Industry Applications*, vol. 47, no. 1, pp. 105-114, Jan.-Feb. 2011, doi: 10.1109/TIA.2010.2090842.
[8] Z. Han, J. Liu, W. Yang, D. B. Pinhal, N. Reiland and D. Gerling, "Improved Online Maximum-Torque-Per-Ampere Algorithm for Speed Controlled Interior Permanent Magnet Synchronous Machine," in *IEEE Transactions on Industrial Electronics*, vol. 67, no. 5, pp. 3398-3408, May 2020, doi: 10.1109/TIE.2019.2918471.
[9] R. Antonello, M. Carraro and M. Zigliotto, "Maximum-Torque-Per-Ampere Operation of Anisotropic Synchronous Permanent-Magnet Motors Based on Extremum Seeking Control," in *IEEE Transactions on Industrial Electronics*, vol. 61, no. 9, pp. 5086-5093, Sept. 2014, doi: 10.1109/TIE.2013.2278518.
[10] N. Bedetti, S. Calligaro, C. Olsen and R. Petrella, "Automatic MTPA Tracking in IPMSM Drives: Loop Dynamics, Design, and Auto-Tuning," in *IEEE Transactions on Industry Applications*, vol. 53, no. 5, pp. 4547-4558, Sept.-Oct. 2017, doi: 10.1109/TIA.2017.2708683.
[11] F. Lin, Y. Liu and W. Yu, "Power Perturbation Based MTPA With an Online Tuning Speed Controller for an IPMSM Drive System," in *IEEE Transactions on Industrial Electronics*, vol. 65, no. 5, pp. 3677-3687, May 2018, doi: 10.1109/TIE.2017.2762634.
[12] J. Wang et al., "An Accurate Virtual Signal Injection Control of MTPA for an IPMSM With Fast Dynamic Response," in *IEEE Transactions on Power Electronics*, vol. 33, no. 9, pp. 7916-7926, Sept. 2018, doi: 10.1109/TPEL.2017.2764500.
[13] X. Zhou, Y. Zhou, H. Wang, M. Lu, F. Zeng and Y. Yu, "An Improved MTPA Control Based on Amplitude-Adjustable Square Wave Injection," in *IEEE Transactions on Energy Conversion*, vol. 35, no. 2, pp. 956-965, June 2020, doi: 10.1109/TEC.2020.2968737.
[14] S. Bolognani, L. Peretti and M. Zigliotto, "Online MTPA Control Strategy for DTC Synchronous-Reluctance-Motor Drives," in *IEEE Transactions on Power Electronics*, vol. 26, no. 1, pp. 20-28, Jan. 2011, doi: 10.1109/TPEL.2010.2050493.
[15] M. H. Mahmud, Y. Wu and Y. Zhao, "Extremum Seeking-Based Optimum Reference Flux Searching for Direct Torque Control of Interior Permanent Magnet Synchronous Motors," in *IEEE Transactions on Transportation Electrification*, vol. 6, no. 1, pp. 41-51, March 2020, doi: 10.1109/TTE.2019.2962327.
[16] G. Liu, J. Wang, W. Zhao and Q. Chen, "A Novel MTPA Control Strategy for IPMSM Drives by Space Vector Signal Injection," in *IEEE Transactions on Industrial Electronics*, vol. 64, no. 12, pp. 9243-9252, Dec. 2017, doi: 10.1109/TIE.2017.2711507.
[17] S. Jung, J. Hong and K. Nam, "Current Minimizing Torque Control of the IPMSM Using Ferrari's Method," in *IEEE Transactions on Power Electronics*, vol. 28, no. 12, pp. 5603-5617, Dec. 2013, doi: 10.1109/TPEL.2013.2245920.
[18] Z. Xia, S. Nalakath, R. Tarvirdilu-Asl, Y. Sun, J. Wiseman and A. Emadi, "Online Optimal Tracking Method for Interior Permanent Magnet Machines With Improved MTPA and MTPV in Whole Speed and Torque Ranges," in *IEEE Transactions on Power Electronics*, vol. 35, no. 9, pp. 9753-9769, Sept. 2020, doi: 10.1109/TPEL.2020.2970111.
[19] Y. Jeong, S. Sul, S. Hiti and K. M. Rahman, "Online Minimum-Copper-Loss Control of an Interior Permanent-Magnet Synchronous Machine for Automotive Applications," in *IEEE Transactions on Industry Applications*, vol. 42, no. 5, pp. 1222-1229, Sept.-Oct. 2006, doi: 10.1109/TIA.2006.880910.
[20] H. -S. Kim and S. -K. Sul, "Real-time Torque Control of IPMSM under Flux Variations," in *IEEE Journal of Emerging and Selected Topics in Power Electronics*, to be published, doi: 10.1109/JESTPE.2020.3032463.
[21] A. Varatharajan, G. Pellegrino and E. Armando, "Direct Flux Vector Control of Synchronous Motor Drives: A Small-Signal Model for Optimal Reference Generation," in *IEEE Transactions on Power Electronics*, vol. 36, no. 9, pp. 10526-10535, Sept. 2021, doi: 10.1109/TPEL.2021.3067694.
[22] H. -S. Kim, J. Yoo and S. -K. Sul, "Online MTPA Operation of IPMSM Based on Dual-Loop Control in Polar Coordinates," in *IEEE Transactions on Power Electronics*, vol. 37, no. 4, pp. 4431-4441, April 2022, doi: 10.1109/TPEL.2021.3120405.
[23] W. Xu and R. D. Lorenz, "High-Frequency Injection-Based Stator Flux Linkage and Torque Estimation for DB-DTFC Implementation on IPMSMs Considering Cross-Saturation Effects," in *IEEE Transactions on Industry Applications*, vol. 50, no. 6, pp. 3805-3815, Nov.-Dec. 2014, doi: 10.1109/TIA.2014.2322134.
[24] Y. Lee and S. Sul, "Position-Sensorless MTPA Control of IPMSM Based on High-Frequency Signal Injection," *2019 10th International Conference on Power Electronics and ECCE Asia (ICPE 2019 - ECCE Asia)*, Busan, Korea (South), 2019, pp. 2562-2567.
[25] Q. Tang, A. Shen, P. Luo, H. Shen, W. Li and X. He, "IPMSMs Sensorless MTPA Control Based on Virtual q-Axis Inductance by Using Virtual High-Frequency Signal Injection," in *IEEE Transactions on Industrial Electronics*, vol. 67, no. 1, pp. 136-146, Jan. 2020, doi: 10.1109/TIE.2018.2890487.
[26] Y. Yoon, S. Sul, S. Morimoto and K. Ide, "High-Bandwidth Sensorless Algorithm for AC Machines Based on Square-Wave-Type Voltage Injection," in *IEEE Transactions on Industry Applications*, vol. 47, no. 3, pp. 1361-1370, May-June 2011, doi: 10.1109/TIA.2011.2126552.
[27] H. Kim, S. Sul, H. Yoo and J. Oh, "Distortion-Minimizing Flux Observer for IPMSM Based on Frequency-Adaptive Observers," in *IEEE Transactions on Power Electronics*, vol. 35, no. 2, pp. 2077-2087, Feb. 2020, doi: 10.1109/TPEL.2019.2920691.
[28] J. Yoo, H. -S. Kim and S. -K. Sul, "Design of Frequency-Adaptive Flux Observer in PMSM Drives Robust to Discretization Error," in *IEEE Transactions on Industrial Electronics*, vol. 69, no. 4, pp. 3334-3344, April 2022, doi: 10.1109/TIE.2021.3075854.
[29] C. -E. Hwang, Y. Lee and S. -K. Sul, "Analysis on Position Estimation Error in Position-Sensorless Operation of IPMSM Using Pulsating Square Wave Signal Injection," in *IEEE Transactions on Industry Applications*, vol. 55, no. 1, pp. 458-470, Jan.-Feb. 2019, doi: 10.1109/TIA.2018.2864117.
[30] G. Pellegrino, R. I. Bojoi, P. Guglielmi and F. Cupertino, "Accurate Inverter Error Compensation and Related Self-Commissioning Scheme in Sensorless Induction Motor Drives," in *IEEE Transactions on Industry Applications*, vol. 46, no. 5, pp. 1970-1978, Sept.-Oct. 2010, doi: 10.1109/TIA.2010.2057395.
[31] X. Chen, J. Wang, B. Sen, P. Lazari and T. Sun, "A High-Fidelity and Computationally Efficient Model for Interior Permanent-Magnet Machines Considering the Magnetic Saturation, Spatial Harmonics, and Iron Loss Effect," in *IEEE Transactions on Industrial Electronics*, vol. 62, no. 7, pp. 4044-4055, July 2015, doi: 10.1109/TIE.2014.2388200.
[32] F. Briz, M. W. Degner and R. D. Lorenz, "Analysis and design of current regulators using complex vectors," in *IEEE Transactions on Industry Applications*, vol. 36, no. 3, pp. 817-825, May-June 2000, doi: 10.1109/28.845057.

Jiwon Yoo (S'17) was born in Seoul, South Korea, in 1990. He received the B.S. degree in electrical engineering from Seoul National University, Seoul, South Korea in 2017, where he is currently pursuing the Ph.D. degree in electrical engineering. From 2014 to 2017, He was a Research Engineer with Seoho Electric Company, Anyang, South Korea. His current research interests include power electronics, control of electric machines, power semiconductors, and sensorless drives.

He was the recipient of the Best Paper Award First Prize at 2019 International Conference on Power Electronics (ICPE-Busan/ECCE-Asia) and the Best Paper Award at 2020 International Power Electronics and Motion Control Conference (IPEMC-Nanjing/ECCE-Asia).

Hyeon-Sik Kim (S'14–M'19) was born in Busan, South Korea, in 1988. He received the B.S. and Ph.D. degree in electrical and computer engineering from Seoul National University, Seoul, South Korea, in 2013 and 2019, respectively.

From 2019 to 2021, he was a Principal Research Engineer with Hyundai Mobis, South Korea. Since 2021, he has been with the Gachon University, Seongnam, South Korea, where he is an Assistant Professor. His research interests include electric machine drives, electric/hybrid vehicles, and power electronic systems in various applications. He was the recipient of the 2015 Industrial Power Converter Committee (IPCC) First Prize Paper Award of the IEEE Industrial Application Society.

Seung-Ki Sul (S'78–M'87–SM'98–F'00) received the B.S., M.S., and Ph.D. degrees in electrical engineering from Seoul National University, Seoul, South Korea, in 1980, 1983, and 1986, respectively. From 1986 to 1988, he was an Associate Researcher with the Department of Electrical and Computer Engineering, University of Wisconsin, Madison, WI, USA. From 1988 to 1990, he was a Principal Research Engineer with LG Industrial Systems Company, South Korea. Since 1991, he has been a faculty member with the School of Electrical and Computer Engineering, Seoul National University, where he is currently a Professor. He has authored or coauthored more than 150 IEEE journal papers and a total of more than 340 international conference papers in the area of power electronics. His current research interests include position sensorless control of electrical machines, electric/hybrid vehicles and ship drives, and power-converter circuits based on SiC MOSFET.

Dr. Sul was the Program Chair of IEEE Power Electronics Specialists Conference in 2006 and the General Chair of IEEE International Conference on Power Electronics and ECCE-Asia in 2011. From 2011 to 2014, he was the Editor-in-Chief for the Journal of Power Electronics, an SCIE-registered journal published by the Korean Institute of Power Electronics (KIPE), Seoul, South Korea. For the year 2015, he was the President of KIPE. He was simultaneously the recipient of the 2015 IEEE Transaction 1st and 2nd Paper Awards on Industrial Application. He was also the recipient of the 2016 Outstanding Achievement Award of the IEEE Industrial Application Society. He was also selected as the recipient of the 2017 Newell award sponsored by IEEE Power Electronics Society. For the last 40 years of R &D experience, he involved in over 150 industry-sponsored collaboration projects in the area of elevator drive, steel mill plant, home appliance, PCS of renewables, electric/hybrid vehicles, and ship propulsion.